Acta Materialia 271 (2024) 119883

Contents lists available at ScienceDirect

Acta Materialia

journal homepage: www.elsevier.com/locate/actamat

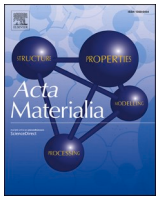

Nano-scale corrosion mechanism of T91 steel in static lead-bismuth eutectic: A combined APT, EBSD, and STEM investigation

Minyi Zhang [a,*], Guanze He [a,b,*], Mark Lapington [b], Weiyue Zhou [c], Michael P. Short [c], Paul A.J. Bagot [a], Felix Hofmann [b,*], Michael P. Moody [a]

[a] Department of Materials, University of Oxford, Parks Road, Oxford OX1 3PH, United Kingdom
[b] Department of Engineering Science, University of Oxford, Parks Road, Oxford OX1 3PJ, United Kingdom
[c] Department of Nuclear Science and Engineering, Massachusetts Institute of Technology, 77 Massachusetts Avenue, Cambridge 02139, MA, USA

ARTICLE INFO

Keywords:
T91
Liquid lead bismuth eutectic
Corrosion
Fast reactor
Nano-scale characterization

ABSTRACT

T91 steel is a candidate material for structural components in lead-bismuth-eutectic (LBE) cooled systems, for example fast reactors and solar power plants [1]. However, the corrosion mechanisms of T91 in LBE remain poorly understood. In this study, we have analysed the static corrosion of T91 in liquid LBE using a range of characterisation techniques at increasingly smaller scales. A unique pattern of liquid metal intrusion was observed that does not appear to correlate with the grain boundary network. Upon closer inspection, electron backscatter diffraction (EBSD) reveals a change in the morphology of grains at the LBE-exposed surface, suggesting a local phase transition. Energy dispersive X-ray (EDX) maps show that Cr is depleted in the T91 material near the LBE interface. Furthermore, we observed the dissolution of all Cr-enriched precipitates in this region. Although the corrosion is conducted in an oxygen deficient environment, both scanning transmission electron microscopy (STEM) and atom probe tomography (APT) reveal a thin surface oxide layer (presumably wüstite) at the LBE-steel interface. Using electron energy loss spectroscopy (EELS) in the STEM, as well as APT, the atomic scale elemental redistribution and 3D morphology of the corrosion interface is investigated. By combining results from these different techniques, several types of oxide phases and structures can be identified. Based on this detailed nano-scale information, we propose potential mechanisms of T91 corrosion in LBE.

1. Introduction

One potential Gen IV nuclear fission reactor concept is the lead-bismuth-eutectic-cooled fast reactor (LBEFR). It would use lead-bismuth eutectic (LBE) as the coolant due to its favourable properties, including low neutron moderation and capture, low melting point, low vapour pressure, wide margin to boiling, excellent gamma radiation shielding, and relatively low reactivity with water or air. These are significant advantages over other potential coolants such as high-pressure water, with the operation pressure and moderation the reactor can hardly be run with a fast spectrum; or sodium (Na) and sodium-potassium alloy (NaK), which ignite spontaneously in air and react explosively with water [2–4].

9Cr-1Mo steels, often denoted T91 or F91, have been proposed as structural components for LBEFRs. In particular, as a ferritic/martensitic (F/M) steel, T91 has excellent resistance to irradiation-induced void swelling [5]. It also has low thermal expansion, high thermal conductivity and a mature supply chain with ASME nuclear qualification [6]. Compared to martensitic steels with higher Cr content, the irradiation-induced ductile-to-brittle transition temperature shift of T91 is lower [7]. Compared to austenitic steels, F/M steels avoid the concern of fast corrosion when temperature is increased above 500 °C promoting ferritization of the austenite [8]. However, liquid metal embrittlement of F/M steel in liquid LBE is a major concern that impedes the use of F/M steels in reactors [9–11]. Liquid metal embrittlement is the reduction in the elongation-to-failure that can be produced when normally ductile solid metals are stressed while in contact with a liquid metal [12]. Because of this, the Multi-purpose Hybrid Research Reactor for High-tech Applications (MYRRHA), designed by SCK-CEN in Belgium, will use 316 L austenitic stainless steel as the structural material [13]. When considering the liquid metal embrittlement of F/M steels in LBE, stress and temperature are two main factors. Liquid metal embrittlement becomes important when the threshold stress is exceeded. Normally it is most prominent just above the melting point of the liquid metal, and as

* Corresponding authors.
E-mail addresses: minyi.zhang@materials.ox.ac.uk (M. Zhang), guanze.he@materials.ox.ac.uk (G. He), felix.hofmann@eng.ox.ac.uk (F. Hofmann).

https://doi.org/10.1016/j.actamat.2024.119883
Received 14 September 2023; Received in revised form 6 March 2024; Accepted 31 March 2024
Available online 2 April 2024

temperature increases further the ductility will gradually return. According to previous studies, for liquid LBE, it mainly happens in the temperature range 300 °C to 500 °C [14].

This paper focusses on the corrosion of T91 in LBE, specifically its mechanism as evidenced by morphological observations of corrosion, to help predict its onset and extent. Corrosion of containment and structural materials remains the main critical issue for LBEFR design [15]. Lead alloys are more corrosive to structural steels than other potential fast reactor coolants like helium or sodium. Furthermore, because of the higher solubility of Fe, Cr, and Ni in liquid LBE compared to liquid lead, material dissolution problems are more severe in LBE than in lead at similar temperatures [16]. Higher temperatures are also known to further exacerbate corrosion [17–19]. When considering the influence of the enhanced effects of LBE, detrimental phase changes, and magnetite/wüstite oxide phase transition regardless of the type of steel selected, whether it be austenitic or F/M, the operation temperature of the reactor generally has to be restricted to ~550 °C or lower. This restriction in turn limits the power density of the reactor and thus economic benefits promised by LBEFR. For example, the Russian LBEFR, SVBR, is limited to 390 °C and the MYRRHA reactor is designed to operate at 400 °C [20]. To help break this bottleneck, and better understand the processes involved, this study investigates T91 samples exposed to static LBE corrosion at 715 °C. At this temperature liquid metal embrittlement could be largely avoided, however these conditions are also known to be highly corrosive to the material. Few studies have investigated LBE corrosion of T91 under these conditions.

Several previous investigations have shown that during corrosion in an oxidizing environment (i.e. oxygen levels sufficient to oxidise iron) an oxide layer is formed at the T91 and LBE interface [21,22]. However, even in a reducing environment, an oxide layer with thickness of around tens of nanometres at the corrosion interface has been observed in a model Fe-12Cr-2Si alloy though it is mainly consisted of Si oxide [23]. This is important, as the oxide layer prevents the direct contact between liquid and underlaying metals, thereby potentially offering some protection against LBE corrosion. However, according to these previous studies, for FeCr alloys, even in an oxygen-saturated environment, the effective protection of the oxide layer (mainly CrO) will reduce with increasing temperatures. The oxide phase transition from dense magnetite to porous wüstite could be a reason for this [24]. At the same time, oxygen content will also influence the protection. Since passivation is not easily achievable at higher temperatures (for this study, it is 715 °C), operating under reducing conditions is a potential alternative. Interestingly a previous study observed shallower LBE ingress into T91 under reducing conditions than in an oxidising environment [25]. Moreover, even in oxidising environment, it is practically challenging to avoid having spots with lower oxygen contents. As such, a detailed understanding of LBE corrosion of T91 under reducing conditions is important.

According to previous studies, the corrosion of materials in LBE with low oxygen level is driven by the dissolution of alloying elements in the liquid LBE [26,27]. A better understanding of how different elements behave in the vicinity of the lead-steel interface is essential to disentangle the mechanisms most important for degradation and to develop strategies to mitigate corrosion. To this end, high resolution characterisation is required. However, thus far the corrosion of F/M steels in liquid LBE or lead has mostly been studied at the microscale [8,21,28,29]. There is little research on the lead corrosion mechanisms within steel at the atomic scale. In this study we consider T91 steel samples exposed to static corrosion in liquid LBE for various lengths of time (70, 245, or 506 h) in a reducing environment at 715 °C. Atom probe tomography (APT) is used to provide precise 3D nanoscale information within key areas of interest within the microstructure related to the corrosion process. APT is coupled with transmission electron microscopy (TEM) and scanning transmission electron microscopy (STEM) equipped with electron energy loss spectroscopy (EELS) and energy-dispersive x-ray spectroscopy (EDX) to characterise nano-scale material morphology and chemistry [30]. Scanning electron microscopy (SEM) combined with EDX allows these observations to be interpreted within the broader microstructural perspective of the corrosion. As a result, investigation of the static corrosion of T91 steel in LBE can be conducted across multiple length scales, and some of the most prominent mechanisms identified.

2. Experiments

2.1. Materials

T91 is a F/M steel purchased in the quenched and tempered condition (provided by Edelstahl Witten-Krefeld GmbH). The T91 material was sectioned by wire electrical discharge machining (EDM) to dimensions of 25 mm x 25 mm x 3–4 mm. All samples were produced from the same bar. One surface of each sample was polished to a mirror finish with the last step of 50 nm alumina suspensions, while the other face was ground with 120 grit SiC paper. The composition specified by the manufacturer is listed in Table 1. APT analysis was conducted on the as-received T91. The average measured composition is reported in Table 1. For the most part the measured composition agrees well with the nominal values. Deviations in the measured values are observed for V, C, N, P, and Nb. V exists in the steel incorporated into precipitates, mostly combined with nitrogen. In the nanoscale volumes inspected by the APT analyses only few precipitates were sampled. However, in other APT analyses of the same/similar (different heat treatment) material, large VN precipitates were observed (see supplementary figure S1). Similarly, Nb, P, and C, are all predominantly associated with carbides (see supplementary figure S2).

Ultra-pure (99.999 wt %) lead and bismuth were purchased from Surepure Chemetals, Inc. and mixed according to a eutectic composition of lead (44.5 *at* %) and bismuth (55.5 *at* %).

2.2. Static corrosion test

The T91 samples were lowered into liquid LBE for static corrosion using a Ti rod, to which they were attached with Mo wires. Two holes near the top edges of the samples were used to fix their orientation and ensure submersion in the LBE. The LBE was contained in 56 mm inside diameter alumina crucibles from McDanel Advanced Ceramics Technologies. The crucibles were enclosed in a stainless steel autoclave, sealed by copper gaskets with knife edges. The autoclave defined the experimental volume with the controlled atmosphere. Details of the experimental configuration are provided elsewhere [31].

The argon and hydrogen used as the cover gas were purified and mixed to a hydrogen concentration of 0.25 % or 2500 ppm. The gas mixture was delivered to the autoclave to lower the oxygen potential during the corrosion testing. The moisture leaving the autoclave was measured and used to calculate the oxygen potential, using the known hydrogen concentration in the gas stream, since the oxygen potential was below the measuring range of oxygen sensors. During the static corrosion testing, the moisture level in the outlet stream was around 2.5 ppm, and thus the hydrogen to moisture ratio around 1000. The corresponding oxygen potential was smaller than 10^{-26} atm, and falls between the equilibrium oxygen potential of Fe_3O_4 and $FeCr_2O_4$ at the testing temperature [31].

The temperature of the LBE was monitored with a K-type thermocouple immediately outside the alumina crucible. The autoclave was heated by a cylindrical furnace from The Mellen Company, Inc. The autoclave was first heated up to around 400 °C for around 12 h to ensure the mixing of LBE and to allow the gas atmosphere to reach a stable state. Next, the autoclave was heated up to 715 °C, and the samples were inserted for different durations of 70, 245, and 506 h, respectively. At the end of the exposure the samples were retracted and cool down inside the furnace. The furnace was shut down to allow the system to cool down. It took around 18 h to reach 40 °C. Samples were cleaned using

Table 1
Composition from the certificate of the T91 material and APT-measured composition (wt %).

	Fe	Cr	Mo	Si	Mn	Ni	V	Cu
Nominal	89.0	8.76	0.93	0.34	0.50	0.30	0.20	–
APT	89.7	7.91	0.88	0.39	0.48	0.30	0.11	0.11
	C	**N**	**P**	**S**	**Al**	**Nb**	**Ga**	
Nominal	0.091	0.052	0.017	0.003	0.008	0.070	0	
APT	0.002	0.013	0.009	–	0.001	0.001	0.04	

acetone to remove organic impurities, but were not cleaned to remove adhered LBE. They were then mounted in Bakelite in cross-section at 90 ° to the original, LBE-exposed surface facing outside. The cross-section samples were then ground with SiC grinding paper to 2500 grit and polished with diamond polishing liquid to 1 μm. Colloidal 50 nm silica polishing was the final preparation step.

2.3. Characterization techniques

The morphology of the cross-sections of the corroded samples was examined by SEM using a dual beam Zeiss NVision 40 FIB-SEM. Microscale chemical composition of the liquid metal attack channels and the matrix was probed by EDX on a Zeiss Merlin FEG-SEM equipped with a Bruker XFlash FlatQUAD 5060F EDX detector, using a working distance of 15–18 mm and an electron beam voltage of 20 kV. Electron Backscatter Diffraction (EBSD) maps were obtained at a working distance of 18 mm and a sample tilt of 70°, with a beam voltage of 20 kV and 5–10nA probe current on Zeiss Merlin FEG-SEM equipped Bruker e-flash high-resolution EBSD detector.

A plan-view TEM sample was prepared using a Zeiss NVision 40 FIB-SEM, following the approach presented by Lozano-Perez [32]. The TEM sample was lifted out onto a Cu grid, then thinned using 30 kV Ga ions to under 100 nm with ion currents ranging from 700 pA to 40 pA. The final step used 2 kV, 200 pA Ga ion polishing to remove surface defects induced by the 30 kV Ga ions. STEM images were recorded using a Jeol ARM 200F cold-FEG TEM operating at 200 kV, fitted with a 100 mm^2 Centurion EDX detector and Gatan GIF Quantum 965 ER, allowing for EDX and EELS map acquisition in regions of interests. The step size for the EDX and EELS maps was 5 nm.

On-axis Transmission Kikuchi Diffraction (TKD) analysis of the TEM sample used a Zeiss Merlin FEG-SEM equipped with a Brucker e-flash high-resolution EBSD detector with an Optimus TKD head. The sample was held normal to the electron beam at a working distance of 5.4 mm and Kikuchi patterns were captured beneath the sample with a horizontal phosphor screen. An electron beam accelerating voltage of 30 kV was used. The step size was 6 nm, and TKD data was processed using the Esprit 2.3 software.

APT samples were prepared using a dual beam Zeiss Crossbeam 540 FIB-SEM. The samples were first trenched and then lifted out and attached to standard silicon micro tip coupons purchased from Cameca. Next, annular FIB milling was used to mill the samples into sharp needles with tip diameter <100 nm. An acceleration voltage of 30 kV was used for FIB milling, followed by a final low energy polishing step (2 kV, 200 pA) to remove FIB-induced surface damage. APT samples were analysed using a Cameca LEAP 5000XR atom probe. A laser energy of 60 pJ, temperature of 50 K, pulse frequency of 125 kHz, and detection rate of 0.4 were used. For Pb-containing samples we found that a pulse rate of 125 kHz or less should be used, as higher pulse rates caused excessive detection loss of Pb ions. The APT data was analysed using AP Suite 6 with the needle shape estimated using the voltage reconstruction[33]. Mass spectrum peak overlap issues were resolved using AtomprobeLab [34,35].

3. Results

3.1. Microstructure and chemical composition analysis of cross-section samples

3.1.1. Morphology of corroded T91

The respective corrosion microstructures of samples associated with different LBE exposure times are presented in Fig. 1(a), (d), and (g). The micrographs show a cross-section, with the LBE-exposed surface on the right-hand side, as indicated in Fig. 1(a). The 506 h exposed sample shown in Fig. 1(g) was directly polished from cross-section at 90 ° to the original without being mounted in Bakelite. However, this resulted in a slightly curved edge after grinding and polishing, as can be seen on the right side of Fig. 1(g). Thus, all subsequent samples were mounted in Bakelite to maintain sharp edges. The corrosion penetration depth was measured as the distance from the original face of the sample to the feature exhibiting maximum LBE penetration. The liquid metal attack channels are similar in shape and protrude deeper into the material with longer corrosion time. This is consistent with the observations reported by Short et al. [23].

Micro-scale elemental re-distribution due to LBE corrosion is revealed by SEM EDX. Fig. 1(b) shows significant Cr depletion ahead of the LBE corroded regions in the sample exposed for 70 h. In contrast, Fe in Fig. 1(c) surrounding the LBE channels exhibits no apparent depletion. Cr depletion alone cannot account for the volume taken up by LBE in the channel, suggesting that Fe is also removed by LBE attack. Furthermore, in Fig. 1(b), the Cr-enriched precipitates that are clearly visible in the non-corroded matrix, on the left side of the image, all appear to have dissociated in the Cr depleted region. As a point of comparison, Fig. 1(j) shows the Cr distribution in the as-received T91 sample, indicating that the subsurface depletion of Cr is an effect caused by LBE exposure. The EDX for 245 h and 506 h exposed samples shows similar results as presented in Fig. 1(e), (f), (h), and 1 (i).

The separation of Pb and Bi at room temperature is detected as shown in Fig. 1(b), (c), (e), (f), (h), and (i). This is expected, as a result of the formation of a Bi-rich phase (γ) and an intermetallic phase (β) below 123.5 °C (the solidus) for Pb-Bi mixtures with eutectic composition [36]. This is indicated in Fig. 1(c) and Fig. 1(l). Local quantitative EDX analyses were undertaken for different phases marked by the dashed blue circles in Fig. 1(c). The measured EDX composition of Bi rich phase (phase γ) is 91.2 wt. % Bi and 8.8 wt. % O. For intermetallic phase (phase β), it has 56.9 wt. % Pb, 35.1 wt. % Bi, and 8.0 wt. % O. A similar two-phase microstructure in the LBE region is also found at higher magnification using TEM, shown in Fig. 1(k) and (l).

3.1.2. Depletion of CR and FE in the corroded region

The different depletion behaviour of Cr and Fe is characterised using SEM EDX. Fig. 2(a) shows an SEM EDX map for the liquid metal attack channels with Cr depletion at a larger scale. The white box corresponds to the region of interest that is shown enlarged in Fig. 2(b). For quantitative analysis an SEM EDX line scan was applied as indicated by the white line in Fig. 2(b). Based on the Cr content, the area in Fig. 2(b) can be roughly divided into three regions: (1) the T91 matrix, which is yet to be influenced by the LBE; (2) the depletion region, where the depletion of Fe and Cr takes place, and (3) the LBE region, where all Fe and Cr are depleted and only LBE can be found. The original surface of the T91

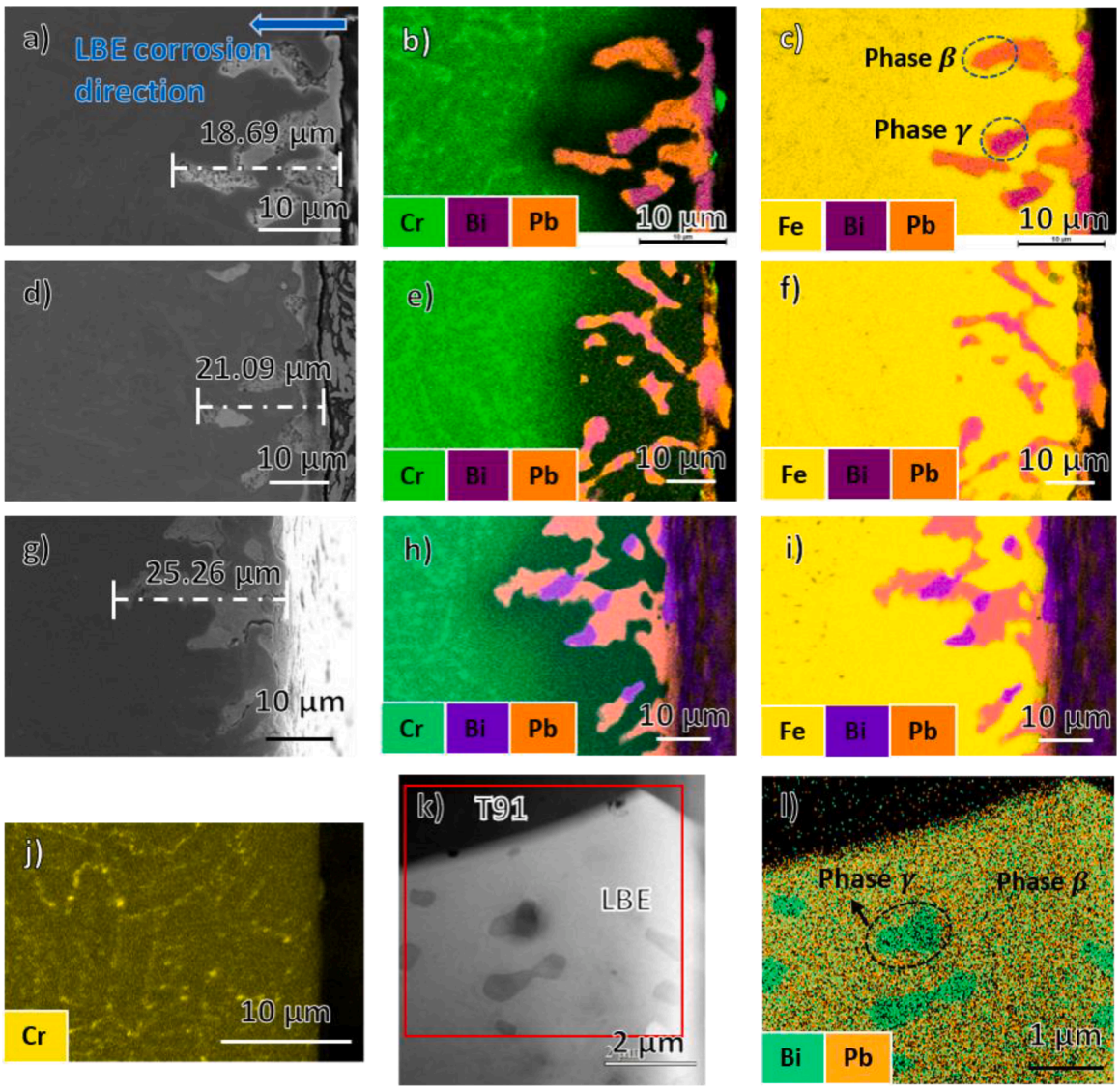

Fig. 1. Cross section SEM micrographs for samples exposed to LBE corrosion for: (a) 70 h at 715 °C, (d) 245 h at 715 °C, and (g) 506 h at 715 °C. SEM-EDX micrograph shows Cr, Bi, and Pb for samples exposed to LBE corrosion for (b) 70 h at 715 °C, (e) 245 h at 715 °C, and (h) 506 h at 715 °C. SEM-EDX micrograph shows Fe, Bi, and Pb for samples exposed to LBE corrosion for (c) 70 h at 715 °C (highlighting the Bi-rich phase (γ) and an intermetallic phase (β) in LBE), (f) 245 h at 715 °C, and (i) 506 h at 715 °C. (j) SEM-EDX map of as-received T91 with Cr shown. (k) STEM HAADF showing features in the LBE region from the sample corroded at 715 °C for 506 h. (l) STEM-EDX showing Pb and Bi in the red box region of (k) highlighting the Bi-rich phase (γ) and an intermetallic phase (β).

sample is set to be the 0 μm reference point. The boundary between the uninfluenced T91 matrix and the original surface is at an approximate depth of 35 μm in the 506 h corroded sample. According to the EDX line scan profile in Fig. 2(b), if only considering the concentration along this line, the Cr content gradually decreases from ~ 9 % in the steel matrix to ~0 % at the LBE-steel interface across the 35 μm depth range. In comparison, the Fe content drops sharply from ~ 90 % to almost 0 % over the much smaller distance of ~1 μm from the LBE-steel interface. Interestingly the EDX map in Fig. 2(b) shows that Cr depletion occurs to a roughly constant distance into the T91 steel, even though the LBE has penetrated to varying depths at different positions along the surface which is likely because there are LBE corrosion channels just outside the plane of this cross section (either deeper in the metal or the region which is polished away).

The gradual depletion of Cr was also measured by APT. In total 8 APT specimens were lifted out from the positions shown in Fig. 2(c), with 5 of these successfully providing data in the subsequent analyses. All of the sampled regions were found to be homogenous, with the exception of APT specimen 3, which contained 2 small VN precipitates (APT reconstructions for these samples are provided in supplementary figure S3). The Cr content measured by APT at each of the respective depths below the surface is plotted in Fig. 2(d), superimposed upon the SEM EDX line scan that was conducted on the same region. The linear interpolation of the APT results matches well with the EDX measurements, providing some cross-validation for the Cr concentrations determined by SEM EDX.

3.1.3. *Grain morphology change near LBE-exposed surface*

EBSD was carried out for as-received T91 and corroded samples, respectively. The IPFZMap of as-received T91 (Fig. 3(a)) shows that the matrix is mainly composed of martensite with a lath structure [36]. After the liquid LBE corrosion (Fig. 3(b)), the grains near LBE intrusions exhibit a somewhat rounder shape, rather than a lath structure. However, the grain morphology on the left side of Fig. 3(b) closely matches that of a sample of the as-received material which has experienced the same heat treatment but without exposure to the corrosive environment. This suggests that a restructuring or a phase change occurs in T91 near the corrosion region that is the result of high temperature LBE corrosion.

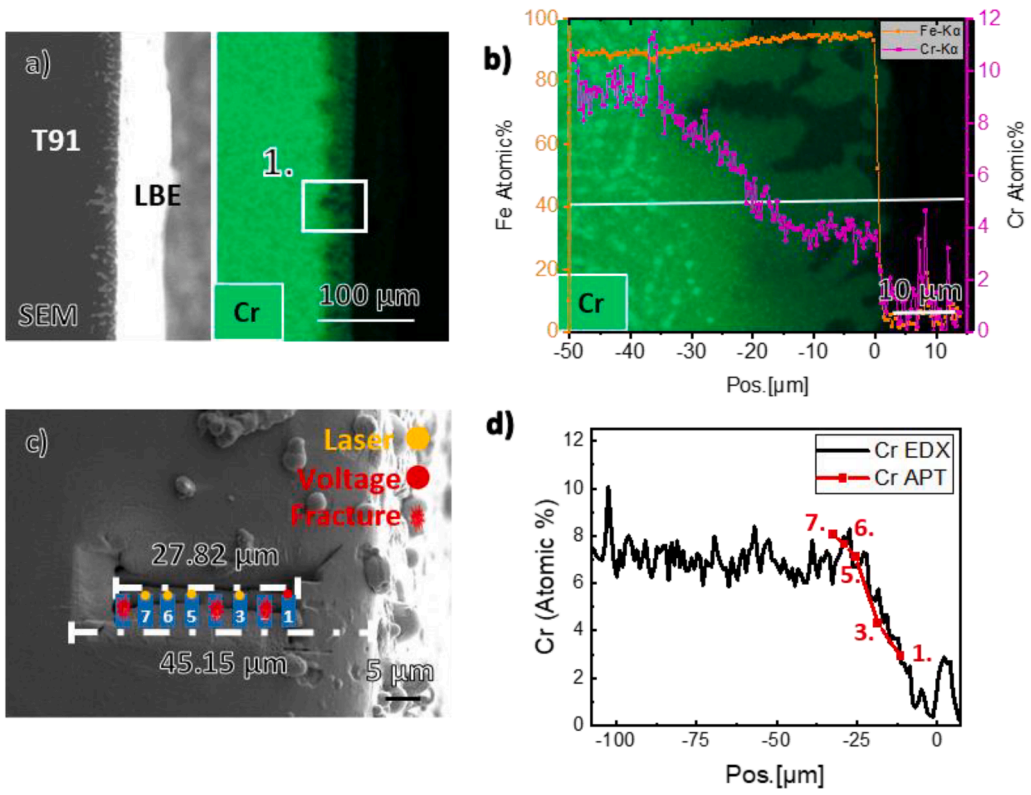

Fig. 2. EDX and APT analysis of Cr depletion in the 506 h, 715 °C, LBE corrosion sample: (a) SEM image and Cr - EDX map for a large cross section area. (b) EDX map for the white box in part (a). The superimposed white line shows the position of the EDX line scan measurement. Plots of Fe and Cr content along the line scan are superimposed. (c) The APT lift out bar and the sample positions. The samples that provided data are numbered. (d) Cr content for the same areas of APT lift out bar from EDX line scan and APT samples in (c).

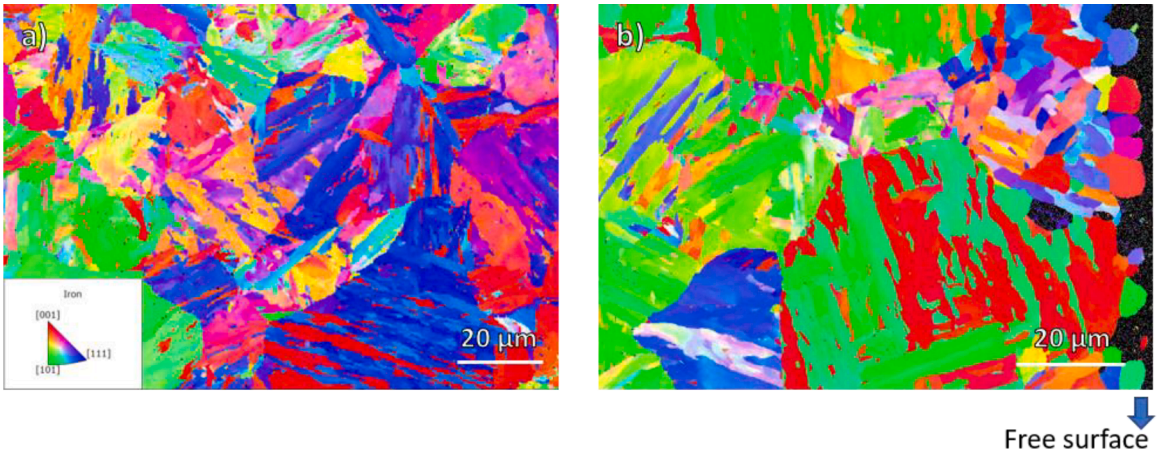

Fig. 3. EBSD examination of sample cross-sections: (a) EBSD IPFZ map for as-received T91. (b) EBSD IPFZ map for 506 h, 715 °C, LBE corrosion sample.

3.2. Nano-to-atomic scale characterization of the LBE and T91 interface

To further examine the structure and chemical composition of the interface between LBE and T91 matrix, two sets of APT samples and a plan view TEM sample were prepared. Nano-to- atomic scale analytical TEM (STEM), APT, and on-axis TKD were carried out.

3.2.1. Grain scale LBE corrosion of T91 steel

Fig. 4(a) presents a cross-section SEM view of the 506 h corroded sample. The porous areas are LBE, the progression of which appears to have been halted by particular grain boundaries. The same morphology can also be seen in Fig. 3(b). A TEM sample was extracted from the area protected by carbon deposition in Fig. 4(a). Fig. 4(b) shows a STEM overview of the TEM sample. The bright area is LBE, while the darker region corresponds to the T91 matrix. From the contrast between different phases, there is no visible LBE penetration into surrounding grain boundaries. This is surprising, since several previous corrosion studies observed grain boundaries to corrode preferentially. Their higher density of defects and less ordered atomic arrangement, compared to the material matrix, promotes faster dissolution of elements into the coolant [37]. As a result, grain boundaries have been previously observed to be preferentially attacked by the coolant, manifested through the formation of thin, elongated corrosion patterns [38]. To further confirm that LBE attack in T91 does not preferentially

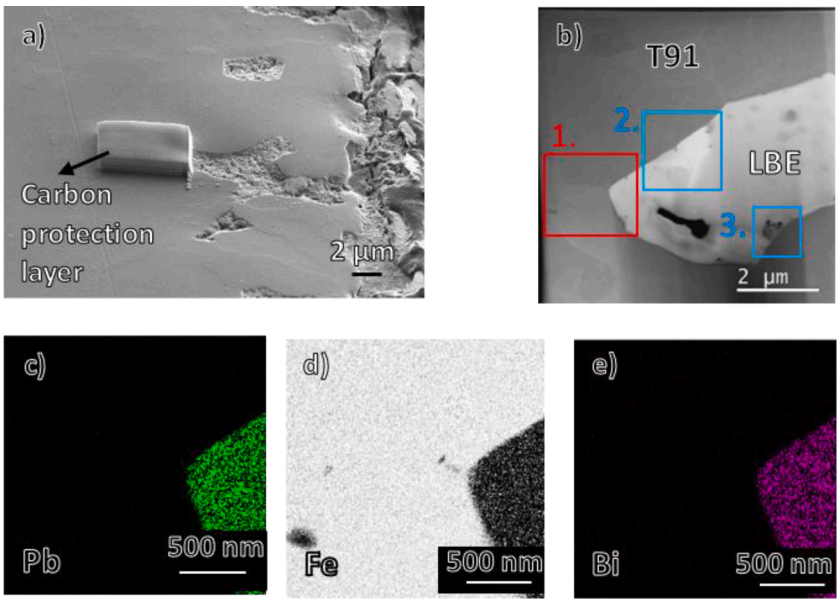

Fig. 4. TEM imaging of 506 h, 715 °C, LBE corrosion sample: (a) SEM view showing the location from where the TEM lift out sample was taken (underneath the carbon protection layer) relative to the bulk sample. (b) STEM HAADF view of the TEM lift out foil. The bright region is LBE, while the dark region is the T91 matrix. EDX mapping was carried out in the red box and the corresponding maps of certain elements are shown in (c) Pb, (d) Fe, and (e) Bi.

progress via infiltration of grain boundaries, STEM-EDX was carried out on the area marked by red box 1 in Fig. 4(b). The results are shown in Fig. 4(c), (d), and (e). While there are several grain boundaries surrounding the LBE region, neither Pb nor Bi penetrate along any of these. At the same time, Fe remains evenly distributed in the T91 matrix without depletion. These observations lead us to hypothesise that LBE corrodes the T91 matrix in a grain-by-grain fashion, resulting in thick channels of liquid metal attack, rather than nano-scale infiltration along grain boundaries. The rationale for, and proposed mechanism of, Fe dissolution into the LBE following Cr dissolution in the LBE will be reviewed thoroughly in the Discussion section below.

Two corroded regions of particular interest can be identified in the TEM sample which are marked with blue boxes in Fig. 4(b). Fig. 5(a), a detailed view of blue box 2 in Fig. 4(b), shows a Fe-rich region, highlighted by the red dashed curve, in the LBE. The interface between T91 steel and LBE is marked by a straight dashed yellow line. According to the EDX results in Fig. 2, the LBE region is expected to have no Fe and high levels of Pb, respectively. However, the EDX maps in Fig. 5(b) and (c) clearly indicate a substantial Fe content still in the LBE-rich region. This suggests a partly corroded grain, before the Fe content (and therefore the entire grain) is fully removed by the LBE.

Fig. 5(d) shows a detailed view of the region highlighted by blue box 3 in Fig. 4(b). Here a multi-phase structure can be seen. The corresponding EELS results, in Fig. 5(e), show that this structure contains negligible Fe. Instead, EELS analysis in Fig. 5(f) reveals the presence of a thin oxygen-enriched layer at the interface of LBE and T91 matrix. The

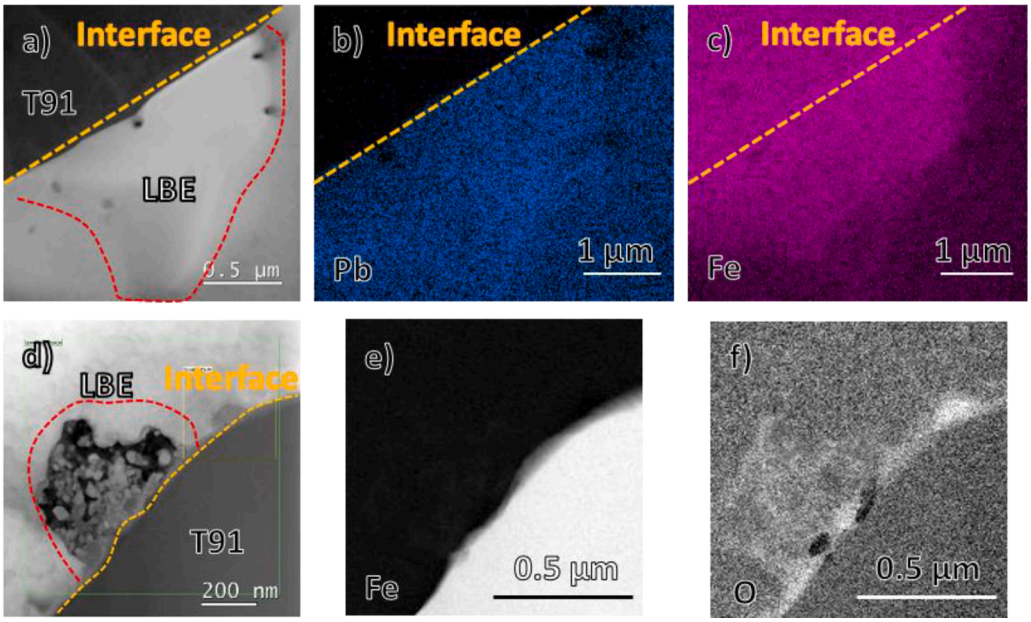

Fig. 5. STEM investigation of two regions of interest in Fig. 4(b): (a) shows a STEM HAADF image corresponding to blue box 2 in Fig. 4, (b) and (c) show the EDX maps of Pb and Fe respectively. (d) shows a STEM HAADF image corresponding to blue box 3 in Fig. 4, (e) and (f) show the EELS maps of Fe and O respectively.

EDX results from the same area further corroborate the EELS results and are included in supplementary figure S4.

3.2.2. Oxide layer at the corrosion interface

Fig. 5(f) shows an oxygen-rich layer at the interface of LBE and T91 matrix. Detailed analysis is carried out using STEM imaging, EDX, EELS and APT, respectively. A representative STEM low-angle annular dark field (LAADF) image is presented in Fig. 6(a), with several further examples included in supplementary figure S5. Fig. 6(a) shows an interface thickness of ~50 nm. The thickness varies depending on position, but is generally on the order of tens of nanometres.

Spectroscopic analysis of the interface is reported in Fig. 6(b), (c) and (d). Fig. 6(b) shows a STEM high-angle annular dark field (HAADF) image taken close to the interface, where the dark region corresponds to the uncorroded T91 grain and the bright region corresponds to the LBE-rich area. An EDX line scan was carried out across the interface along the arrow in Fig. 6(b). The results, shown in Fig. 6(c), suggest that a layer of Fe oxide has been formed at the interface. This is further confirmed by the comparison of EELS core loss spectra, shown in Fig. 6(d), recorded in the two locations marked in Fig. 6(b). The core loss spectrum comes from the energy loss due to interaction between the incident electrons and the inner shell electrons of the elements in the specimen [39]. The excitation of the specimen electrons depends on two states, the initial state that is characteristic to specific elements, and the final state that depends on the local bonding environment. Therefore, a shift of several eV of the core loss edge will be identified for atoms of the same elements but of different valence states [39]. The energy shift of the Fe L3 edge in Fig. 6(d) indicates that the Fe found in region 2 has been oxidised to a higher valence state than the unoxidised Fe found in region 1 [40].

However, from the STEM and EELS results, it is difficult to determine the nature of the oxide and oxide distribution at the interface. Thus, APT was used to further analyse the LBE T91 interface in the 506 h, 715 °C corrosion sample. An interfacial oxide layer, consistent with the observations in Fig. 6, is also present in the APT data. Fig. 7(a) shows the distribution of Fe, Pb, O, and Cr ions in the 3D APT reconstruction. The reconstructed sample exhibits a three-layer structure with LBE as the top layer, a thin oxygen-enriched layer in the middle, and the T91 steel matrix at the bottom. (A video of the APT reconstruction can be found in supplementary video SV1). Fig. 7(b) and (c) show the distribution of detected complex Fe oxide ions and Cr oxide ions. Note that APT reconstructions in Fig. 7(b) and (c) have been rotated anticlockwise by 90° compared to Fig. 7(a). The detection of complex ions is an artefact of the APT experiment and the form of ions observed does not necessarily imply information about the material phase from which they were evaporated [33]. By comparing Fig. 7(b) and (c), several conclusions can be reached: Firstly, Fe oxide ions are distributed relatively uniformly throughout the interface, while Cr oxide ions tend to accumulate in specific areas. Secondly, locations with an increased presence of Cr oxide have less Fe oxide. Inspection of the distribution of other metal oxide ions, such as Ni and V, show higher concentrations at the same locations as Cr oxide ions. This data can be viewed in supplementary figure S6. Fig. 7(d) is a proximity histogram (proxigram) analysis showing how elemental concentrations change across the oxide from LBE to T91 matrix. In this proxigram analysis, a Pb iso-concentration value of 60 at. % is chosen to define the position of the LBE-oxide interface (i.e. 0 nm on the proxigram) with a 1 nm bin size for each step in the histogram. The thickness of the Fe depleted region is ~26 nm, which agrees with the rapid drop in Fe content as measured by SEM-EDX (Fig. 2(b)), and confirms the much shorter depletion distance of Fe compared to Cr. The thickness of the oxide layer measured by APT (~32

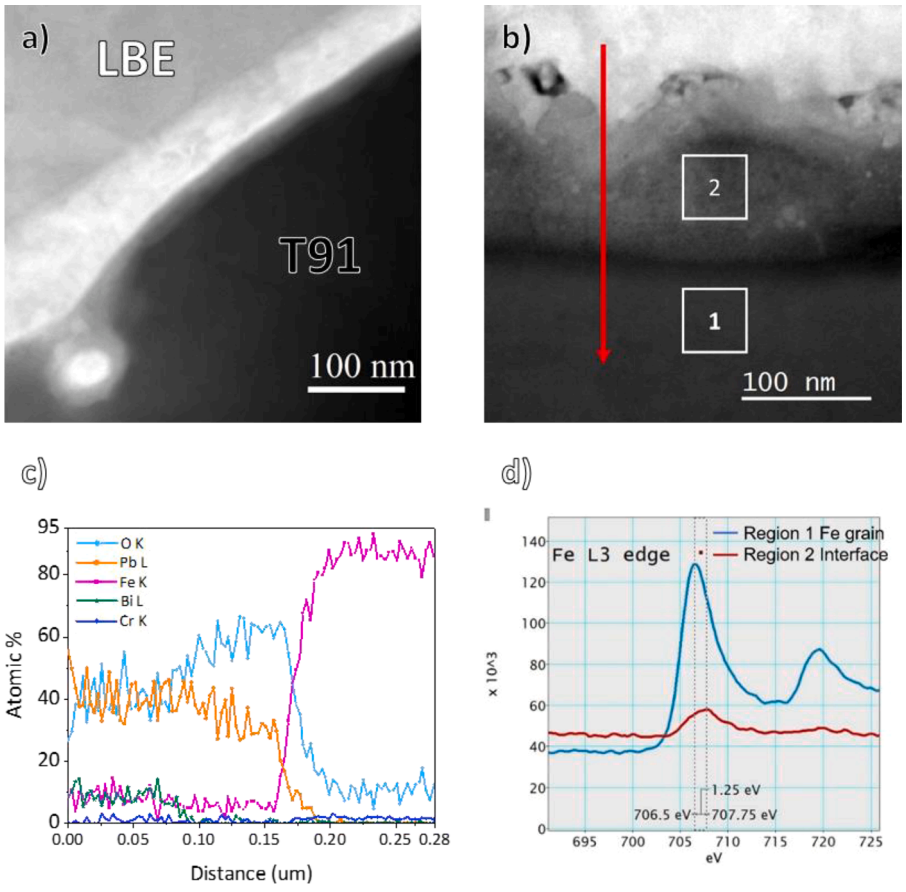

Fig. 6. Oxide layers at the interface between LBE and T91: (a) (b) STEM micrographs of interfacial oxide layers in two different sample regions. (c) EDX line scan along the red arrow in (b). (d) Comparison of EELS spectra extracted from regions 1 and 2 in (b).

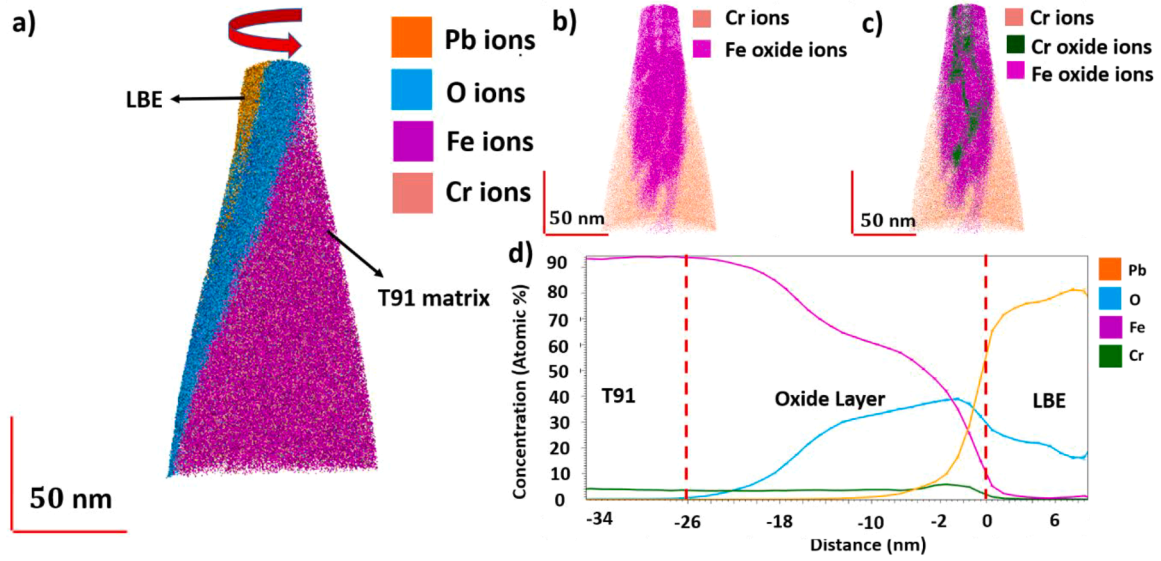

Fig. 7. APT characterisation of the LBE – T91 interface: (a) 3D APT reconstruction showing Pb, Cr, Fe, and O ions. (b) 3D APT reconstruction showing iron oxide and Cr ions. (c) 3D APT reconstruction showing iron oxide, chromium oxide, and Cr ions (d) Proxigram showing elemental concentration changes normal to the T91 – LBE interface (Pb isoconcentration value = 60 at. %).

nm) is in good agreement with the thicknesses determined by STEM in Fig. 6(a) and (b).

APT enables further nanoscale analysis of the microstructure within the oxide layer [41]. Fig. 8(a) highlights the region where Cr oxide ion concentration is higher than 5.5 at. % within the APT sample. We observe Cr oxide ions in two distinct types of structures that appear to correspond to distinct, newly formed small oxide phases or segregation at grain boundaries. Different Cr-oxide-ion-enriched structures, marked by the pink circles in Fig. 8(a), are investigated in detail by comparing the local composition. Compositions were measured in three blue, cuboidal ROIs created within different structures marked by pink circles (see Fig. 8(a)). The measured compositions are listed in table 2 and plotted in Fig. 8(d) with the as-received T91 measured by APT (table 1) also presented. Region 1 in Fig. 8(a), represents a possible Cr oxide phase formed during corrosion; region 2 corresponds to a grain boundary segregation; Region 3 measures the composition of the surrounding oxide material as a reference. The composition results in Fig. 8 (d) show that region 1 is mainly composed of Cr and O with relatively low Fe content and high Mn content compared to regions 2 and 3. The Pb content is also very low in this region. For region 2 the main constituents are O and Fe. The Cr content is lower than in region 1, but still significantly higher than in the surrounding oxide measured in region 3. Region 2 also contains more Pb than the other two areas. In region 3, i.e. the surrounding oxide phase, there is a very limited amount of Cr and Mn. The Pb content is less than in region 2 but still significant. Comparison of the chemical composition in the three regions, suggests that they correspond to different types of structures. Region 1 most likely represents the Cr oxide phase formed on the surface. However, due to the low oxygen content and lack of Cr, it forms a discontinuous structure, rather than a layer of chromium oxide across the surface. Mn accumulation in the Cr oxide phase is shown in Fig. 8(b). Fig. 8 (c) provides the Bi distribution within the sample. Interestingly, more Bi ions are incorporated in the Cr oxide phase than the surrounding areas. This can be stated with some certainty, since there are no overlap issues between Bi and Cr oxide ions in the APT mass spectrum.

3.2.3. *V-enriched precipitates at the corrosion interface*

EDX mapping was applied to the opposite side of the entire TEM sample in Fig. 4(b). The results in Fig. 9(a) show a population of V-enriched precipitates. Compared to the Cr-enriched precipitates in Fig. 1 (b), Fig. 1(e), Fig. 1(h) and Fig. 2(b) that disappear from the Cr-depletion region, it is apparent that the V-enriched precipitates are more resistant to LBE corrosion. Our observations suggest that the density of V-enriched precipitates is higher at the T91 and LBE interface than in other areas. On-axis TKD was used on the area marked with a red rectangle in Fig. 9(a) to identify different phases based on their crystal structure. In Fig. 9(b) V-precipitates appear as yellow, which corresponds to a cubic, rock-salt crystal structure. VC and VN have the same space group and very similar lattice parameters, which makes it challenging to distinguish them using TKD. Fig. 9(c) and (d) show EELS analysis corresponding to Fig. 5(d). They confirm that the precipitates are vanadium-rich nitrides. In the set of APT samples lifted out near the corroded interface (Fig. 2(c)), one sample contained V-enriched precipitates that were found to be V nitride based on the APT mass spectrum analysis. Fig. 9(e) shows the APT analysis of this sample, and Fig. 9(f) provides a proxigram analysis, with the interface defined by a VN iso-concentration of 0.83 at % of VN with 0.1 nm bin size for the histogram. The proxigram analysis suggests that these V nitrides contain higher Nb content than in the surrounding matrix, i.e. the right side of the profile represents composition of the VN precipitate, with concentration of Nb ~ 5 at. %, whereas left side is T91 matrix, with Nb content ~ 0 at. %.

4. Discussion

4.1. *Cr removal from the T91 matrix*

To explore the mechanisms underpinning the observations presented in this study, we first focus on the behaviour of Cr in the corroded T91. According to the dissolution speed of elements in T91, as observed in previous studies and verified here, Cr diffuses from further distance within the T91 to dissolve into liquid LBE in comparison to Fe [23]. When the steel is in contact with liquid LBE, Cr starts to dissolve into the LBE from both grain boundaries and matrix. Grain boundaries can act as fast diffusion paths according to literature [37], though no preferential Cr removal from grain boundaries was observed in this paper. The Cr depletion in the surrounding matrix induces the dissociation of local Cr-enriched precipitates both at prior-austenite grain boundaries and martensite block boundaries. This process can be observed in Fig. 1(b), (e), (h) and Fig. 2(a), (b) which show the Cr depletion and precipitate dissociation, consistent with previous observations [42]. From the line scan in Fig. 2(b), the start of Cr precipitates dissolution corresponds to only a slight drop in the surrounding Cr matrix content below

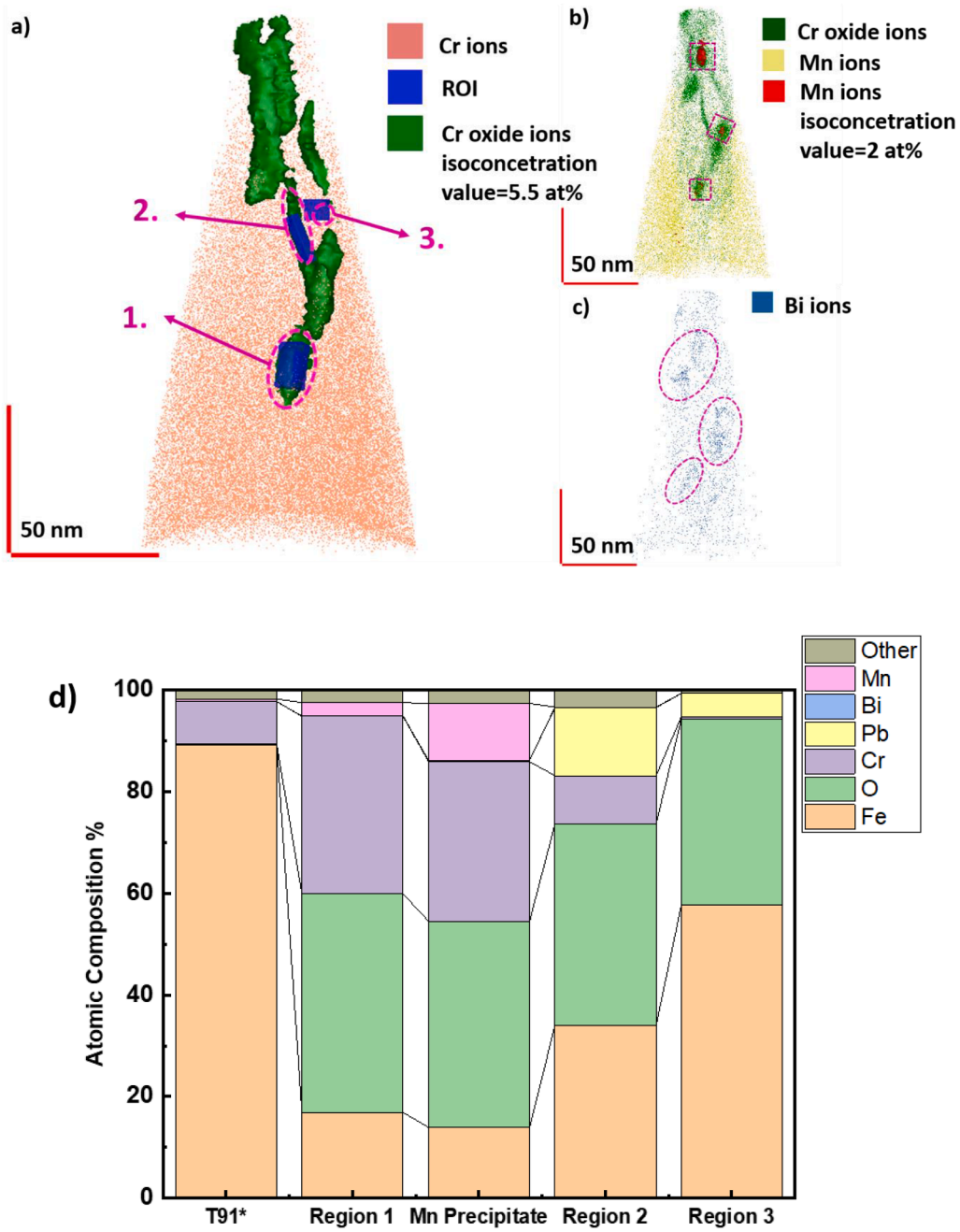

Fig. 8. Detailed analysis of Cr oxide structures in the APT reconstruction: (a) APT 3D reconstruction with different chromium oxides highlighted. (b) APT 3D reconstruction with Mn-enriched precipitates. (c) APT 3D reconstruction showing Bi. (d) concentration of 3 ROI highlighted in Fig. 8(a), Mn precipitates, and as-received T91 listed in Table 1.

Table 2
Compositions of different regions of the APT sample shown in Fig. 7 and 8.

Atomic Percent (%)	Region 1	Region 2	Region 3	Mn precipitate
O	43.01	39.65	36.61	40.56
Cr	34.96	9.52	0.42	31.41
Fe	16.86	33.96	57.69	13.94
Mn	2.66	0.02	0	11.20
Ni	1.40	1.72	0.31	1.18
V	0.33	0.63	0	0.35
Co	0.27	0.10	0.06	0.49
Mo	0.06	0.82	0.18	0.10
Pb	0.04	13.41	4.60	0.24
Bi	0	0.07	0.024	0

approximately 8 at. %. In future it would be interesting to investigate the stability of Cr-containing precipitates as a function of the matrix Cr content from a theoretical perspective. After the Cr precipitates dissociate, residual Cr in the matrix further diffuses to and dissolves into the LBE, leading to the Cr concentration gradient near the T91-LBE interface seen in Fig. 2(b).

In the present geometry the Cr concentration difference is fixed (from 9 at. % in the matrix to ~0 at. % at the LBE-T91 interface as per EDX linescan). The depletion depth is measured from the deepest LBE intrusion (~0 at. % Cr) to the position where the Cr concentration returns to the bulk value of 9 at. %. Fig. 1(d), (e), (h) and Fig. 2(b) show a similar Cr depletion depth of ~5 μm for both 506 h and 70 h corroded samples. This suggests that the Cr depletion depth from the furthest LBE ingress is roughly constant as a function of time. This is further

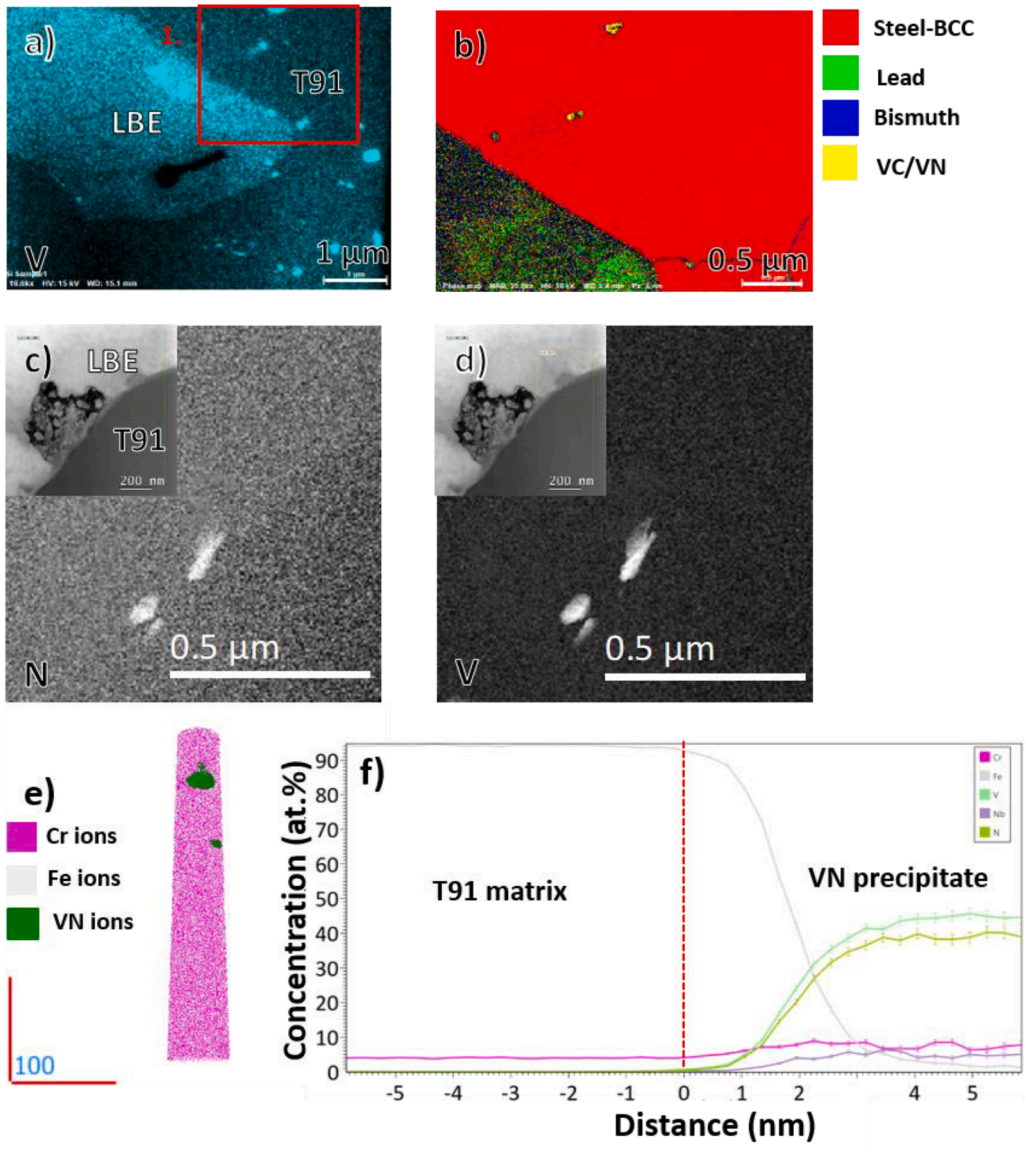

Fig. 9. Detailed analysis of V-rich precipitates near the LBE T91 interface: (a) TEM-EDX for V on the sample examined in Fig. 4(b). (b) on-axis TKD phase map for the red box 1 in Fig. 9(a). (c), (d) STEM-EELS for N and V on the sample examined in Fig. 5(d), also shown inset. (e) 3D APT reconstruction of a liftout sample containing a V-enriched precipitate (also can be found in supplementary figure S3 (b)). (f) Proxigram centred on the interface between the T91 matrix and the V-enriched precipitate in (e).

confirmed by systematic EDX scans that all show similar depletion depths across a range of different positions on the sample surface and for different exposure times, respectively (see supplementary figure S7). The concentration gradient can be approximated by the concentration difference across the depletion depth. Thus, samples exposed for different lengths of time have similar Cr concentration gradient. This could be qualitatively explained by the following mechanism: The Cr dissolution speed is expected to decrease as the concentration gradient decreases, i.e. as the depletion depth increases. As more and more Cr is dissolved, the Cr dissolution rate will eventually reduce to a level at which the ratio of dissolution of Cr and Fe remains approximately constant. Fe dissolves into the liquid LBE resulting in the very steep concentration gradient seen in Fig. 2(b). Thus, a steady state develops, with an approximately constant Cr depletion distance from the moving interface associated with LBE intrusions.

4.2. *Preferential path for LBE corrosion*

Our characterisation shows that LBE corrosion advances through attack patterns of thick liquid intrusions (e.g. Fig. 1 and Fig. 4). This corrosion mechanism is different to that observed in previous studies of molten salt corrosion [43–45] and even some previous studies of LBE corroded austenite [15,19,46] and ferrite/martensite [22,47]. The corrosion of molten salt has been previously observed as a preferential attack of grain boundaries. The underlying mechanism is de-alloying of Cr from the steel matrix, with a preferential intrusion of molten salt as a thin layer following grain boundaries. Austenite was observed corroded with large area ferritization. Our LBE corrosion results show no clear correlation of LBE intrusions with grain boundaries. The width of the liquid LBE intrusions is around 2 µm, which is similar to the typical width of martensite lath blocks or packets in T91 [48]. The surprisingly consistent width of corrosion channels suggests a characteristic length scale. Furthermore, from the STEM HAADF image in Fig. 4(b), the LBE liquid attack channel does not show any local penetration along grain

boundaries. This is very different to the wetting of grain boundaries observed e.g. in molten salt attack [49]. Instead, in the case of LBE, where grain boundaries meet the LBE interface, a blunt corrosion front is seen. Fig. 4(c) also shows that there is no lead or bismuth detected in the surrounding grain boundaries meeting the LBE.

Interestingly, larger scale characterisation showed that there is some correlation of corrosion channels with prior austenite grain boundaries [25]. Overall, a picture emerges where there is no wetting of grain boundaries by the LBE, but where we do see LBE corrosion progress more quickly in regions of high disorder, e.g. triple junctions and prior austenite grain boundaries.

4.3. Oxide layer at corrosion interface

Both the STEM results in Fig. 5, Fig. 6, and the APT analysis in Fig. 7, independently confirm the formation of a thin oxide layer (10 s of nm) at the interface of LBE and T91 matrix in the 506 h corroded samples. According to literature, an oxygen content in excess of 10^{-6} wt. % and temperatures below 600 °C [50,51] are required for the formation of a passivating oxide layer. Thus, passivation is not expected in the present case because the oxygen content in the LBE in this experiment is 1.8×10^{-9} wt. % and the temperature is 715 °C. Rather we observe the formation of discontinuous Cr oxide islands within the thin layer of Fe-rich oxide (see Fig. 8). In addition, because of the Cr dissolution in LBE, the Cr content at the interface is low, which may further contribute to the discontinuous Cr oxide growth.

The corrosion experiment took place in reducing conditions, as indicated by the Ellingham diagram [23,52], which predicts that the environment lacks oxygen to spontaneously form iron oxides. Instead, Fe-Cr-O is predicted as the only Fe-containing oxide to form. However, according to the TEM-EDX line scan result in Fig. 6(c) and APT results in Fig. 7(d), the interface contains approximately equal amounts of Fe and O with only a low Cr content. High Cr content structures are only detected in some parts of the oxide layer, as shown in Fig. 8. According to literature, when the temperature is higher than 570 °C, magnetite (Fe_3O_4) will transform to wüstite (FeO) [53]. Thus, we propose that the oxide layer is likely wüstite rather than Fe-Cr-O. For the static corrosion conditions of T91 investigated in this study, the combination of low Cr content and limited reaction time may promote the formation of wüstite. Because wüstite is porous [54], Fe and Cr can diffuse through it into the LBE. Similarly, the LBE can still penetrate through the wüstite, contact the T91 matrix and thus continue to further corrode the steel. As a result, some grains will simultaneously incorporate high levels of both Pb and Fe during the corrosion process, as seen in the partly corroded grain in Fig. 5(a). In addition, Fig. 5(d) shows an oxide region surrounded by LBE. This suggests that, as the corrosion front moves forward, the oxide layer may become detached, rather than moving with the steel/LBE interface.

5. Conclusion

In this study, the static corrosion of T91 in high-temperature, low-oxygen liquid LBE was investigated. Using APT, TEM, EELS, EDX, EBSD and SEM, we have characterised the micro- and nano-scale morphology and composition of the LBE ingress and the LBE-T91 interface. From this, the following mechanistic insights and conclusions can be reached:

For the LBE attack pattern: In the process of liquid LBE corrosion, the intrusion of the corrosion front does not appear to correlate preferentially with the grain boundary network. The Cr depletion adjacent to the corrosion interface is much larger in scale than that observed for Fe. At the same time, in the Cr depletion region, Cr-enriched precipitates are dissolved. Furthermore, markedly different grain morphology is observed in the near-LBE region. This suggests that there may be a LBE-induced phase change of T91, though this requires further investigation.

At the interface formed between LBE and T91: The corrosion of T91 in liquid LBE in reducing environment is a combination of oxidation and elemental dissolution. The thin oxide layer formed is likely FeO (wüstite), with other phases also appearing in a variety of structures. VN precipitates possess much higher resistance in liquid LBE than Cr precipitates.

Based on our observations, we propose the following corrosion sequence:

- Cr initially preferentially dissolves from T91 into in liquid LBE creating a depilation zone adjacent to the corrosion interface.
- Cr precipitates dissociate in the region adjacent to the interface corresponding to the drop in Cr content.
- The rate of Cr dissolution eventually slows, relative to that of Fe, with decreasing concentration gradient
- Constant Fe and Cr dissolution rates are reached which promotes the development of a stable Cr depletion distance.
- Fe dissolution into LBE progresses in a grain-by grain fashion.

Declaration of competing interest

The authors declare that they have no known competing financial interests or personal relationships that could have appeared to influence the work reported in this paper.

Data availability

Zhang, Minyi, He, Guanze, Lapington, Mark, Zhou, Weiyue, Short, Michael, Bagot, Paul, Hofmann, Felix, & Moody, Michael. (2023). Data for 'Nano-scale corrosion mechanism of T91 steel in static lead-bismuth eutectic: A combined APT, EBSD, and STEM investigation' [Data set]. Zenodo. https://doi.org/10.5281/zenodo.8341129.

Acknowledgements

EP/T002808/1, Simultaneous Corrosion/Irradiation Testing in Lead and Lead-Bismuth Eutectic: The Radiation Decelerated Corrosion Hypothesis (RC-3).

EP/T011505/1, An Atomic-Scale Characterisation Facility for Active Nuclear Materials.

NEUP 19-16754, Simultaneous Corrosion/Irradiation Testing in Lead and Lead-Bismuth Eutectic: The Radiation Decelerated Corrosion Hypothesis.

EP/R010145/1, The authors acknowledge use of characterisation facilities within the David Cockayne Centre for Electron Microscopy, Department of Materials, University of Oxford, alongside financial support provided by the Henry Royce Institute.

Supplementary materials

Supplementary material associated with this article can be found, in the online version, at doi:10.1016/j.actamat.2024.119883.

References

[1] N. Lorenzin, A. Abanades, A review on the application of liquid metals as heat transfer fluid in Concentrated Solar Power technologies, Int. J. Hydrogen. Energy 41 (17) (2016) 6990–6995.
[2] J. Van den Bosch, Liquid metal embrittlement susceptibility of ferritic–martensitic steel in liquid lead alloys, J. Nuclear Mater. 376 (3) (2008) 322–329.
[3] J. Zhang, N. Li, Review of the studies on fundamental issues in LBE corrosion, J. Nuclear Mater. 373 (1–3) (2008) 351–377.
[4] D. Gorse, Influence of liquid lead and lead–bismuth eutectic on tensile, fatigue and creep properties of ferritic/martensitic and austenitic steels for transmutation systems, J. Nuclear Mater. 415 (3) (2011) 284–292.
[5] F.A. Garner, M.B. T, B.H. Sencer, Comparison of swelling and irradiation creep behavior of fcc-austenitic and bcc-ferritic/martensitic alloys at high neutron exposure, J. Nuclear Mater. 276 (1–3) (2000) 123–142.

[6] T.P. Davis, Atom probe characterisation of segregation driven Cu and Mn–Ni–Si co-precipitation in neutron irradiated T91 tempered-martensitic steel, Materialia (Oxf) 14 (2020).
[7] A. Kohyama, Low-activation ferritic and martensitic steels for fusion application, J. Nuclear Mater. 233 (1996) 138–147.
[8] Y. Kurata, S. Saito, Temperature dependence of corrosion of ferritic/martensitic and austenitic steels in liquid lead-bismuth eutectic, Mater. Trans. 50 (10) (2009) 2410–2417.
[9] I. Proriol Serre, J.B. Vogt, Liquid metal embrittlement sensitivity of the T91 steel in lead, in bismuth and in lead-bismuth eutectic, J. Nuclear Mater. 531 (2020).
[10] X. Gong, Liquid metal embrittlement of an Fe10Cr4Al ferritic alloy exposed to oxygen-depleted and -saturated lead-bismuth eutectic at 350°C, Corros. Sci. 165 (2020).
[11] P. Gordon, H.H. An, The mechanisms of crack initiation and crack propagation in metal-induced embrittlement of metals, Metallurgical Trans. A 13 (3) (1982) 457–472.
[12] M.G. Nicholas, C.F. Old, Review Liquid metal embrittlement, J. Mater. Sci. (14) (1979) 1–18.
[13] O. Klok, Liquid Metal Corrosion Effects in MYRRHA Candidate 316L Austenitic Stainless Steel, Vrije Universiteit Brussel, 2018.
[14] V. Tsisar, Long-term corrosion performance of T91 ferritic/martensitic steel at 400 °C in flowing Pb-Bi eutectic with 2 × 10−7 mass% dissolved oxygen, Corros. Sci. (2020) 174.
[15] P. Hosemann, Twin boundary-accelerated ferritization of austenitic stainless steels in liquid lead–bismuth eutectic, Scr. Mater. 118 (2016) 37–40.
[16] T.R. Allen, Materials challenges for generation IV nuclear energy systems, Nucl. Technol. 162 (3) (2017) 342–357.
[17] K. Wolski, V. Laporte, Grain boundary diffusion and wetting in the analysis of intergranular penetration, Mater. Sci. Eng.: A 495 (1–2) (2008) 138–146.
[18] N. Marie, K. Wolski, M. Biscondi, Intergranular penetration and embrittlement of solid nickel through bismuth vapour condensation at 700 C, J. Nuclear Mater. 296 (1–3) (2001) 282–288.
[19] K. Lambrinou, Dissolution corrosion of 316L austenitic stainless steels in contact with static liquid lead-bismuth eutectic (LBE) at 500°C, J. Nuclear Mater. 490 (2017) 9–27.
[20] D. Jalůvka, G. Van den Eynde, S. Vandewalle, Development of a core management tool for MYRRHA, Energy Convers. Manage 74 (2013) 562–568.
[21] F. Barbier, Compatibility tests of steels in flowing liquid lead–bismuth, J. Nuclear Mater. 295 (2–3) (2001) 149–156.
[22] G. Benamati, Temperature effect on the corrosion mechanism of austenitic and martensitic steels in lead–bismuth, J. Nuclear Mater. 301 (1) (2002) 23–27.
[23] M.P. Short, R.G. Ballinger, H.E. Hänninen, Corrosion resistance of alloys F91 and Fe–12Cr–2Si in lead–bismuth eutectic up to 715°C, J. Nuclear Mater. 434 (1–3) (2013) 259–281.
[24] D.G. Briceno, Influence of temperature on the oxidation/corrosion process of F82Hmod. martensitic steel in lead–bismuth, J. Nuclear Mater. 303 (2–3) (2002) 137–146.
[25] M. Lapington, Characterisation of corrosion damage in T91/F91 steel exposed to static liquid lead-bismuth eutectic at 700-715°C, J. Nuclear Mater. (2023) 154687.
[26] Y. Kurata, M. Futakawa, S. Saito, Corrosion behavior of steels in liquid lead–bismuth with low oxygen concentrations, J. Nuclear Mater. 373 (1–3) (2008) 164–178.
[27] J. Zhang, Oxygen control technology in applications of liquid lead and lead–bismuth systems for mitigating materials corrosion, J. Appl. Electrochem. 43 (8) (2013) 755–771.
[28] Z. Hadjem-Hamouche, T. Auger, I. Guillot, Temperature effect in the maximum propagation rate of a liquid metal filled crack: the T91 martensitic steel/Lead–Bismuth Eutectic system, Corros. Sci. 51 (11) (2009) 2580–2587.
[29] Y. Kurata, Corrosion behavior of Si-enriched steels for nuclear applications in liquid lead–bismuth, J. Nuclear Mater. 437 (1–3) (2013) 401–408.
[30] K. Bawane, Determining oxidation states of transition metals in molten salt corrosion using electron energy loss spectroscopy, Scr. Mater. 197 (2021).
[31] M. Short, R. Ballinger, H. Hänninen, Corrosion resistance of alloys F91 and Fe–12Cr–2Si in lead–bismuth eutectic up to 715 C, J. Nuclear Mater. 434 (1–3) (2013) 259–281.
[32] S. Lozano-Perez, A guide on FIB preparation of samples containing stress corrosion crack tips for TEM and atom-probe analysis, Micron. 39 (3) (2008) 320–328.
[33] B. Gault, Atom Probe Microscopy. Springer Series in Materials Science, Springer-Verlag, New York, 2012 ed.
[34] A.J. London, Quantifying uncertainty from mass-peak overlaps in atom probe microscopy, in: M.-John Mansfield (Ed.), Microscopy and Microanalysis, Microscopy Society of America, US, 2019, pp. 378–388, 4304 Spring Lake Boulevard|Ann Arbor, Editor.
[35] London, A.J. AtomProbeLab. 2021; Available from: https://sourceforge.net/projects/atomprobelab/.
[36] S. Morito, The morphology and crystallography of lath martensite in Fe-C alloys, Acta Mater. 51 (6) (2003) 1789–1799.
[37] Scully, J.C., Fundamentals of corrosion. 1975.
[38] W. Zhou, Proton irradiation-decelerated intergranular corrosion of Ni-Cr alloys in molten salt, Nat. Commun. 11 (1) (2020) 3430.
[39] R.F. Egerton, Electron Energy-Loss Spectroscopy in the Electron Microscope, Springer Science & Business Media, 2011.
[40] H. Tan, Oxidation state and chemical shift investigation in transition metal oxides by EELS, Ultramicroscopy 116 (2012) 24–33.
[41] M.T. Lapington, Characterization of oxidation mechanisms in a family of polycrystalline chromia-forming nickel-base superalloys, Acta Mater. 206 (2021).
[42] A. Di Gianfrancesco, Materials for Ultra-Supercritical and Advanced Ultra-Supercritical Power Plants, woodhead Publishing, 2016.
[43] B.A. Pint, Characterization of Fe and Cr dissolution and reaction product formation in molten chloride salts with and without impurities, Mater. High Temp. (2023) 1–11.
[44] K.M. Sankar, P.M. Singh, Effect of metal fluorides on the corrosion of structural materials in molten LiF-NaF-KF, Corros. Sci. 213 (2023) 110977.
[45] Y. Yang, One dimensional wormhole corrosion in metals, Nat. Commun. 14 (1) (2023) 988.
[46] C. Schroer, Selective leaching of nickel and chromium from Type 316 austenitic steel in oxygen-containing lead–bismuth eutectic (LBE), Corros. Sci. 84 (2014) 113–124.
[47] V. Tsisar, Characterization of corrosion phenomena and kinetics on T91 ferritic/martensitic steel exposed at 450 and 550°C to flowing Pb-Bi eutectic with 10−7 mass% dissolved oxygen, J. Nuclear Mater. 494 (2017) 422–438.
[48] H. Kitahara, Crystallographic features of lath martensite in low-carbon steel, Acta Mater. 54 (5) (2006) 1279–1288.
[49] L. Jiang, Tellurium segregation-induced intergranular corrosion of GH3535 alloys in molten salt, Corros. Sci. (2022) 194.
[50] M. Popovic, Oxidative passivation of Fe–Cr–Al steels in lead-bismuth eutectic under oxygen-controlled static conditions at 700° and 800°C, J. Nuclear Mater. 523 (2019) 172–181.
[51] A. Weisenburger, Stability of oxide layer formed on high-chromium steels in LBE under oxygen content and temperature fluctuation, in: The 13th International Conference on Nuclear Engineering Abstracts, 2005.
[52] H.J.T. Ellingham, Transactions and Communications, J. Society Chem. Industry 63 (5) (1944) 125–160.
[53] Zhiyuan Chen, K.C. C, Kazuki Morita, Mechanism of metastable wüstite formation in the reduction process of iron oxide below 570°C. 2016.
[54] R. Tien, E. Turkdogan, Gaseous reduction of iron oxides: part IV. Mathematical analysis of partial internal reduction-diffusion control, Metallurgical Trans. 3 (1972) 2039–2048.